Fault Detection in Inverter-Based Microgrids Utilizing a Nonlinear Observer

by

Nathan Carnovale

B.S. Electrical Engineering, University of Pittsburgh, 2019

Submitted to the Graduate Faculty of

the Swanson School of Engineering in partial fulfillment

of the requirements for the degree of

Master of Science in Electrical and Computer Engineering

University of Pittsburgh

2021

UNIVERSITY OF PITTSBURGH

SWANSON SCHOOL OF ENGINEERING

This thesis was presented

by

Nathan Carnovale

It was defended on

March 23, 2021

and approved by

Dr. Brandon M. Grainger, PhD., Assistant Professor,

Department of Electrical and Computer Engineering

Dr. Robert J. Kerestes, PhD., Assistant Professor,

Department of Electrical and Computer Engineering

Dr. Alexis Kwasinski, PhD., Associate Professor,

Department of Electrical and Computer Engineering

Thesis Advisor: Dr. Brandon M. Grainger, PhD., Assistant Professor,

Department of Electrical and Computer Engineering

Fault Detection in Inverter-Based Microgrids Utilizing a Nonlinear Observer

Nathan Carnovale, M.S.

University of Pittsburgh, 2021

Traditionally, rotating machines in the bulk power system have provided enough inertia to result in fault currents that are more than five or six times nominal current. Typical circuit protection schemes are designed to act on this high and long lasting fault current. However, with the growing trend of increased penetration of renewable energy, energy storage and microgrids, power electronic based systems are becoming more widely utilized on the grid. In heavily inverter-based power systems, the difference between nominal currents and short circuit fault currents is minimal due to reduced system inertia which altogether makes fault detection difficult. In this research, a model-based approach that utilizes the assumed dynamics of a grid-tied inverter along with a nonlinear observer is proposed to detect system abnormalities and faults. The goal of this observer is to provide insight into unmodelled signatures present in the system. These signatures in turn can be utilized to identify faults in the system creating a detection scheme. Most importantly, this method requires no additional sensors other than those required by the grid-tied inverter which is a key advantage over many proposed solutions in literature. Through use of the PSCAD simulation environment, a two-inverter system model was developed to reproduce the types of low fault currents described. Line-to-ground and line-to-line faults were then observed and detected at multiple fault locations with the proposed observer to assess its effectiveness of identifying faults in these fault scenarios.

Keywords: fault detection, fault identification, inverter-based generation, microgrid, nonlinear observer.

Table of Contents

List of Tables

List of Figures

Preface

I would like to extend my sincere gratitude to Dr. Brandon Grainger, my advisor, for his guidance throughout not only my graduate, but also undergraduate experience at the University of Pittsburgh. His passion and dedication to his students is unmatched and his guidance was invaluable in this research effort. He has truly been an impactful mentor for both my personal and academic growth. I would also like to thank Michael McIntyre from the University of Louisville. His work with nonlinear observers was a foundational starting point for this work and his help and support throughout was crucial.

I would also like to extend a thanks to Duquesne Light and the IEEE Charles LeGeyt Fortescue Scholarship fund for the financial support which allowed me to dedicate my efforts towards research.

To my fellow graduate students and peers, especially those of the Electric Power Systems Laboratory, I am truly grateful for the time spent working alongside each of you.

Finally, a special thanks to my parents. As electrical engineers, you both were the driving forces behind my interest and passion for electrical engineering and power systems from a young age. I appreciate the support and guidance in helping me to achieve my goals. Thank you for always being there for me. To all of you, I could not have accomplished this without you!

1.0 Introduction

Traditionally, rotating machines in the bulk power system have provided enough inertia to result in fault currents that are more than five or six times nominal current. Typical circuit protection schemes are designed to act on this high and long lasting fault current [1], [2]. However, with the growing trend of increased penetration of renewable energy, energy storage and microgrids, power electronic based systems are becoming more widely utilized on the grid. Power systems that are heavily power electronic based face the challenge of having reduced system inertia which becomes a major concern when dealing with fault detection and identification [3]. In these systems, the difference between nominal currents and short circuit fault currents makes fault detection difficult, as short circuit fault currents often are only in the range of 1.0 to 2.0 p.u [4]. This results in a significant challenge for traditional fault protection methods to effectively identify faults, which is especially concerning given the trend towards increased renewable energy integration.

Proposed solutions to this type of fault detection and identification in literature fall into three groups:

- Identifying unique fault indicators and waveform features with analytic approaches [5], [6], [7], [8].
- Utilizing fast communication techniques, multiple sensors, and synchronized measurements [7], [9].
- Adding equipment to the system to modify microgrid quantities, like system phase angles, to enable use of traditional protection [1], [7].

The change in phase difference between voltage and current in a specific microgrid system scenario is proposed as a fault indicator in [1], and is used to develop a fault detection and fault direction algorithm with additional signal measurements and hardware. In [5], a method using wavelet transformation and Park's vector approach is proposed to achieve microgrid fault detection. An inverter fault model is analytically developed in [6] to attempt to capture and explain the behavior of microgrids in the event of a fault to allow for development of an

appropriate fault detection and protection strategy. The strategy of [8] is highly specific to upstream faults in grid-tied microgrids and proposes the use of voltage and current second order harmonic magnitudes to identify faults. In [9], a method using digital relays with a communication network is proposed to protect the system against faults.

Reference [7] provides a summary of several additional techniques proposed to solve the issues of microgrid fault identification and location which fall into the categories listed above. Several of the methods proposed utilizing a central energy storage system as the main current source in the system, showing that it was able to provide enough fault current for traditional fault protection methods to clear faults. Other proposed methods include additional sensors to detect transient fault signals, feature extraction selection preprocessing methods, machine learning algorithms, microprocessor-based relay communication approaches, the analysis of symmetrical components, and the use of an additional digital central protection unit.

However, these proposed solutions are often custom designed to the system used for development and have several other shortcomings. For instance, distribution networks by nature, are inherently unbalanced. This unbalance causes negative and zero sequence currents to flow even during normal operating conditions. A typically proposed approach is detecting faults using sequence components [7]. However, many microgrids are small distribution networks and detecting sequence currents will not suffice for fault detection as normal unbalanced conditions could be identified as faulted conditions, making the determination between normal conditions and faulted conditions a challenge [10]. Furthermore, some solutions only protect against certain types of faults, are specific to single-phase or three-phase systems, or are only suited for grid-connected or grid-disconnected (islanded) conditions. Many solutions have the disadvantage of being dependent on device communications which adds delay and another fail point to the system. Finally, most proposed solutions are costly as they add multiple additional components to the system [7].

The contribution of this work is a fault detection technique utilizing a model-based nonlinear observer to identify faults in inverter-based power systems with inherently low fault currents which would otherwise be unidentified by traditional fault protection schemes. In particular the goal of the designed observer is to provide insight into unmodelled signatures present in the system. These signatures can then be utilized to identify faults in the system

creating a detection scheme. The main advantage of the proposed solution is that this method requires no additional sensor other than those required by the grid-tied inverter.

The remainder of this thesis is organized as follows. In Section 2, the inverter-based power system model is developed. Section 3 provides the theory behind the nonlinear observer technique for fault detection. Results of fault studies are presented in Section 4. In Section 5, final conclusions and remarks are made.

2.0 System Model

A significant component of this work dealt with developing a working system model to be studied. A system which was heavily-inverter based that would replicate the types of low fault currents seen empirically in real systems was an essential, yet challenging system to reproduce in simulation environments. The main problem is that under fault, the mathematics involved in solving the simulation will force the system sources to produce whatever current is required to feed that fault. This is an issue because it is required that fault currents remain close to their nominal levels. If fault current levels are high, then traditional overcurrent fault protection methods, such as circuit breakers, are a perfect solution. It is the systems in which the semiconductors within inverters clamp the output current levels at 1.0 - 2.0 p.u. where this problem becomes interesting and where the issues described in literature are found. It is, however, a challenge to replicate the real clamping nature of real inverters in a simulation environment while still maintaining steady and stable voltage and frequency values. This was the challenge and motivation for the chosen system created in the PSCAD simulation environment. With multiple systems attempted in various simulation environments, a two-inverter system consisting of a grid-forming inverter, grid-tied inverter, and a feeder branch with multiple line impedances, a transformer, and fixed load was chosen to be developed in PSCAD to provide a system to produce low fault currents and multiple fault locations for testing. The following sections break down the development of each major component of the system, including providing the parameter values used in simulation.

2.1 Overall System Model Development

In order to study the effectiveness of a nonlinear observer on close to nominal fault currents typical of inverter-based power systems, a system that would produce such fault current levels is required. The three-phase, two-inverter system model under study, adapted from a commercial microgrid setup at Eaton's Power Systems Experience Center in Warrendale, PA

studied in [8], is shown in Fig. 1. Designed and implemented in PSCAD, the system model includes a grid-forming inverter, grid-tied inverter, and a feeder branch with multiple line impedances, Δ-Y transformer, and fixed load. The sources are exclusively inverter-based and exhibit the expected low fault current levels.

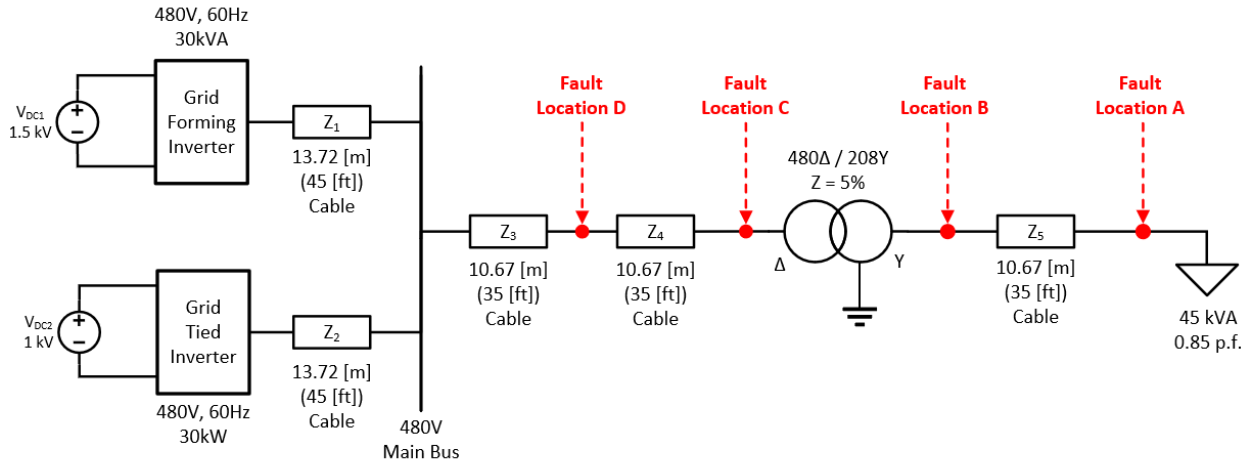

Figure 1: Two-inverter system model under study.

Fig. 1 shows the system model one-line. Note that there are line impedances between each source and the main 480V bus and three line impedances between the main 480V bus and the load. Additionally, in the feeder branch, there is a Δ-Y transformer, which provides another impedance between the sources and loads as well as a phase shift. The line and transformer impedances serve two purposes in the model. First, the multiple impedances provide multiple fault locations to be tested. Namely, fault locations A and B are downstream of the transformer near the load, separated by a single line impedance. Fault locations C and D are on the primary side of the transformer closer to the main 480V bus.

The second purpose of the impedances is to provide a scenario where low fault currents will result without the source voltages collapsing entirely. As more impedance is included between the inverter sources and the fault location, it is expected that the source voltage will not collapse entirely, allowing the sources to remain in operation under fault. For example, if a single phase to ground fault were to occur at the main 480V bus, it would be expected that the voltage in the phase under fault would be approximately zero. If this were the

case, both the grid-forming and grid-tied inverters would trip due to loss of voltage and an additional fault identification technique would not be necessary. The nature of the feeder in this model allows for more interesting test cases in which low fault currents would occur while the inverters are still within the bounds of the operating voltage range.

2.2 Model Components

2.2.1 Grid-Forming Inverter

2.2.1.1 Model

The first main component of the system is the grid-forming inverter. In an inverter-based system isolated or disconnected (islanded) from a main grid source, it is required that one inverter acts as the system master and the remaining sources as system slaves. Therefore, in the two-inverter system model it is imperative that one of the inverters is modelled as a grid-forming source as one inverter is required to set the system voltage and frequency. Fig. 2 shows the model developed in the simulation environment and Table 1 shows the parameters of the grid-forming inverter modelled in PSCAD. In the subsequent subsection, the control of the grid-forming inverter will be addressed directly.

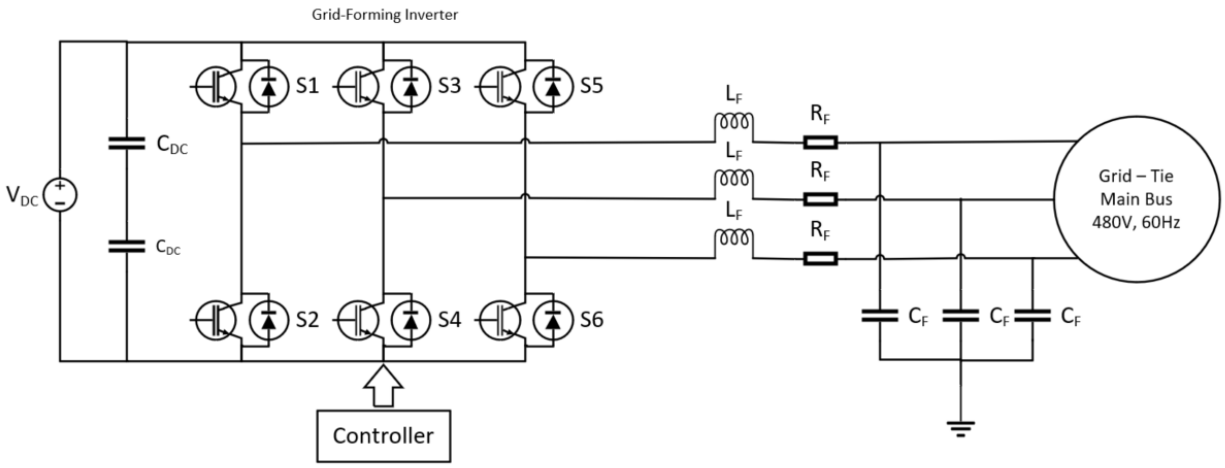

Figure 2: Three-phase grid-forming voltage source inverter model.

Table 1: Grid-Forming Inverter Parameters

Parameter	**Value**
S_{rating}	30 kVA
$V_{AC,LL}$	480 V
f_{rated}	60 Hz
V_{DC}	1.5 kV
C_{DC}	1950 μF
R_F	0.1 Ω
L_F	0.010 H
C_F	100 μF

2.2.1.2 Control

Motivated by [11], the control loops for the grid-forming inverter are shown in Fig. 3. As previously mentioned, in an inverter-based system isolated or disconnected (islanded) from a main grid source, it is required that one inverter source acts as the system master and the

remaining sources as system slaves. The grid-forming inverter takes the role of producing a stable grid voltage and frequency. In the control loop, v^* and ω^* provide the voltage and frequency references, respectively. To replicate the clamping nature of the power electronics within inverters in simulation, the current reference PI controller integrators, PI-1 and PI-2, are regulated to saturate at +/- 1.5 p.u., limiting the D-axis and Q-axis reference parameters, i_d^* and i_q^*. Under fault, the goal of the model of this inverter is to clamp its output current while still maintaining close to nominal voltage and frequency. The modulation signals m_{abc} are sent to a standard pulse-width-modulation (PWM) controller where the modulation signals are compared to triangular wave signal to control the switching in the inverter. The frequency of switching, as well as gains for the PI controllers, and v^* and ω^* references are shown in Table 2. Important to note is that the control is all done in per unit. The voltage and current measurements to provide the feedback loops are immediately per unitized on an $S_{base} = 30$ kVA and $V_{base} = 480$ V.

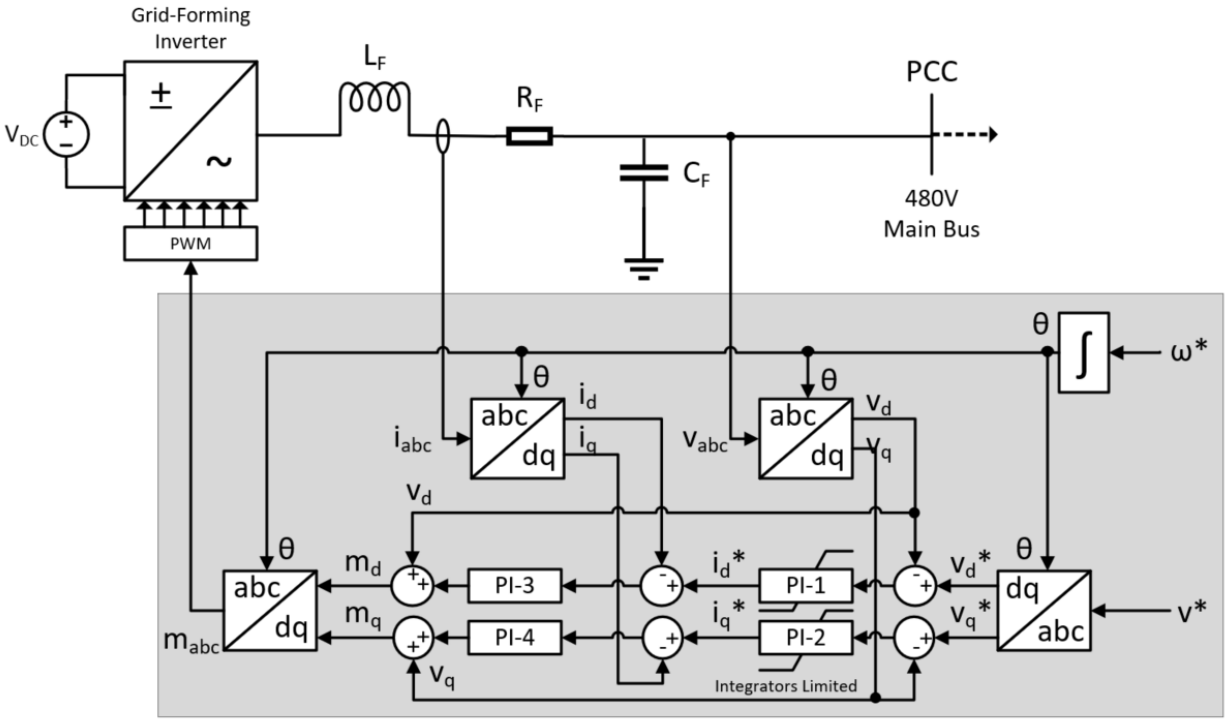

Figure 3: Three-phase grid-forming voltage source inverter producing a sinusoidal voltage determined by a nominal voltage amplitude v^* and reference frequency ω^* [11].

Table 2: Grid-Forming Inverter Control Parameters

Parameter	**Value**
S_{base}	30 kVA
V_{base}	480 V
f_{rated}	60 Hz
$f_{carrier}$	16 kHz
v_d^*	1.0 p.u.
v_q^*	0.0 p.u.
ω^*	1.0 p.u.
k_{P1}, k_{P2}, k_{P3}, k_{P4}	5
k_{I1}, k_{I2}, k_{I3}, k_{I4}	200
$PI-1$ Limits	[-1.5, 1.5]
$PI-2$ Limits	[-1.5, 1.5]

Finally, *Motor Notation*, shown in Fig. 4 was used to calculate the DQ transformation of the three-phase signals in the control loops.

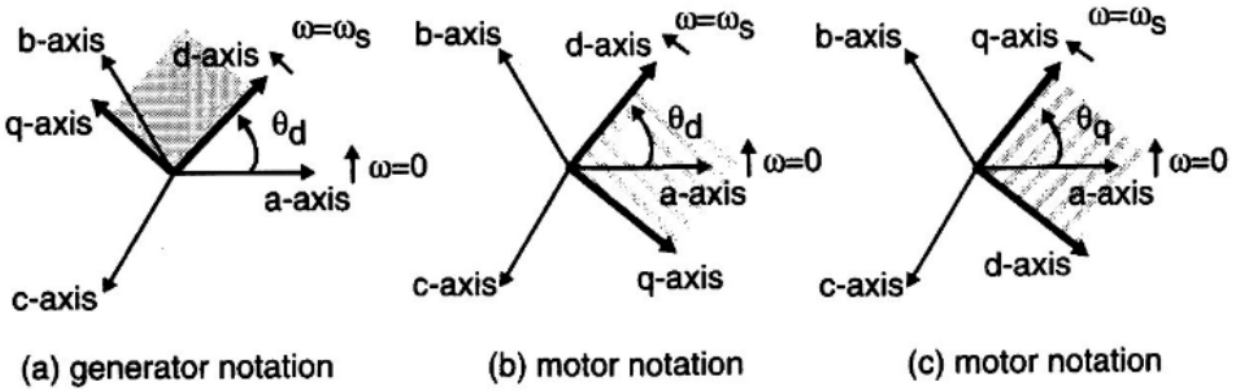

Figure 4: Summary of DQ transformation types [13].

The control responses for D-axis and Q-axis voltage references are shown in Fig. 5. A 1.0 p.u. reference was selected for D-axis voltage and 0.0 p.u. reference for Q-axis voltage

for simplicity. A step reference was used to initialize the inverter at time, t = 0 seconds. As seen in the plots, the control loops adequately respond to step changes in the D-axis voltage with minimal overshoot and quick rise time, while holding the Q-axis voltage constant at zero. In steady state, the error is almost entirely removed. This therefore, verifies the functionality of the grid-forming inverter model under normal conditions which will be used for the subsequent nonlinear observer investigation.

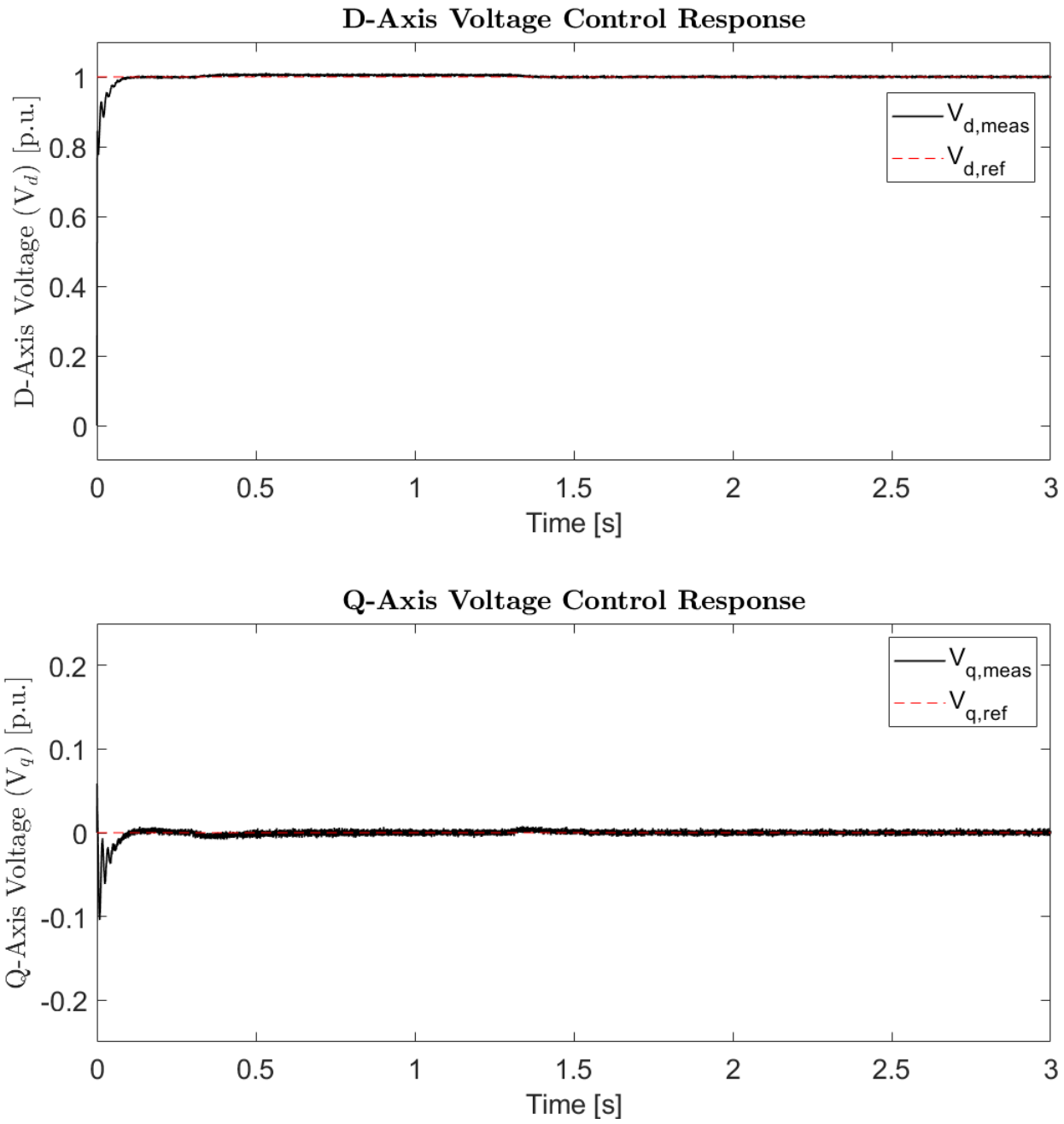

Figure 5: D-Axis and Q-Axis voltage reference step response, grid-forming inverter control.

2.2.2 Grid-Tied Inverter

2.2.2.1 Model

The second main component of the system is the grid-tied inverter. In an inverter-based system isolated or disconnected (islanded) from a main grid source, it is required that one inverter acts as the system master and the remaining sources as system slaves. Therefore, in the two-inverter system model this inverter uses the voltage and frequency set by the grid-forming inverter. Grid-tied inverters are often used in photovoltaic (PV) applications with a string of PV panels providing the DC input voltage to the input. This is the inverter which will be used to simulate and test the nonlinear observers developed in the next chapter. It a simple and common type of inverter and was selected as the inverter under study for those reasons. Fig. 6 shows the model developed in the simulation environment and Table 3 shows the parameters of the grid-tied inverter modelled in PSCAD. In the subsequent subsection, the control of the grid-tied inverter will be addressed directly.

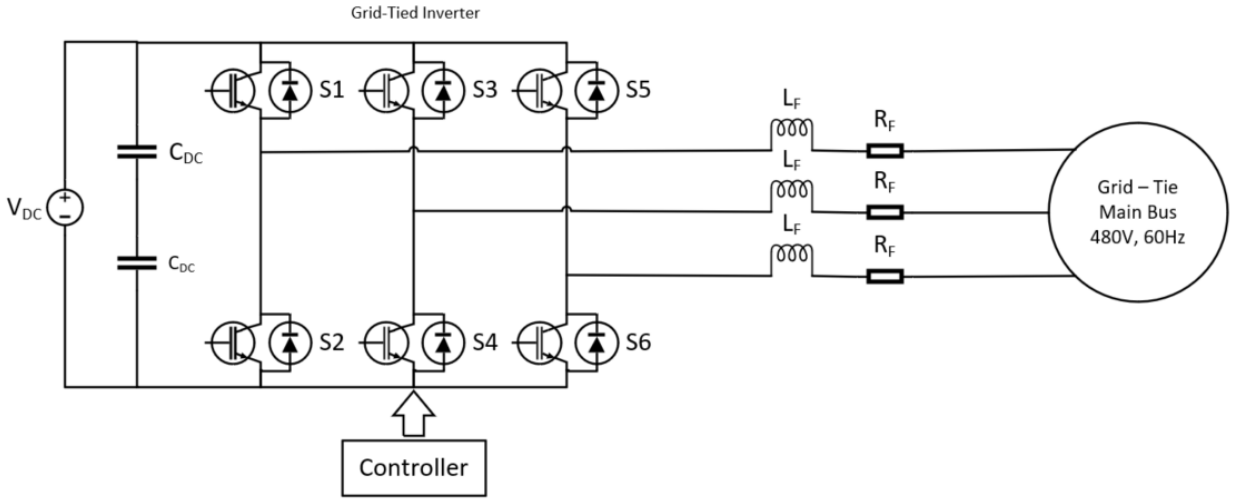

Figure 6: Three-phase grid-tied voltage source inverter model.

Table 3: Grid-Tied Inverter Parameters

Parameter	**Value**
P_{rating}	30 kW
$V_{AC,LL}$	480 V
f_{rated}	60 Hz
$p.f._{rated}$	1.0
V_{DC}	1.0 kV
C_{DC}	1950 μF
R_F	0.1 Ω
L_F	0.010 H

2.2.2.2 Control

Similarly, the control for the grid-tied inverter modelled in Fig. 7 was designed based on a simple grid-tied inverter model with active and reactive power control [12]. The grid-tied inverter synchronizes to a grid reference voltage and frequency created by the grid-forming inverter and requires this grid-forming source in order to operate properly. Typical of the requirements for a solar grid-tied inverter, the inverter under study is commanded to operate close to unity power factor through P^* and Q^* at 1.0 p.u. and 0.0 p.u., respectively. The modulation signals m_{abc} are sent to a standard pulse-width-modulation (PWM) controller where the modulation signals are compared to triangular wave signal to control the switching in the inverter. The frequency of switching, as well as gains for the PI controllers, and P^* and Q^* references are shown in Table 4. Important to note is that the control is all done in per unit. The voltage and current measurements to provide the feedback loops are immediately per unitized on an S_{base} = 30 kVA and V_{base} = 480 V. Finally, *Motor Notation*, shown in Fig. 4 was used to calculate the DQ transformation of the three-phase signals in the control loops.

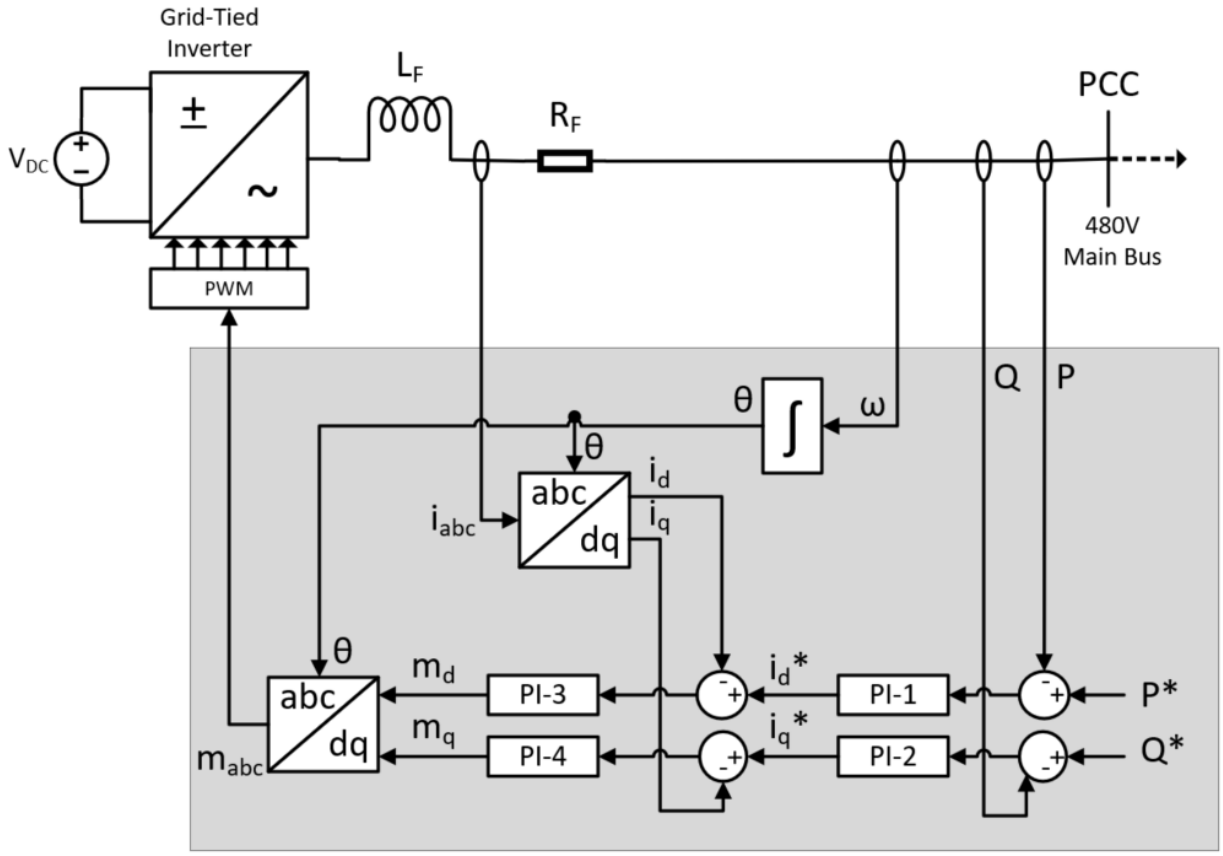

Figure 7: Three-phase grid-tied voltage source inverter with active and reactive power control [12].

Table 4: Grid-Tied Inverter Control Parameters

Parameter	**Value**
S_{base}	30 kVA
V_{base}	480 V
f_{rated}	60 Hz
$f_{carrier}$	16 kHz
P^*	1.0 p.u.
Q^*	0.0 p.u.
k_{P1}, k_{P2}	1
k_{P3}, k_{P4}	5
k_{I1}	20
k_{I2}	10
k_{I3}	500
k_{I4}	33.3

The control responses for active and reactive power are shown in Fig. 8. A 1.0 p.u. reference was selected for active power, P, since it is required of grid-tied solar inverters to operate at unity power factor. Hence, 0.0 p.u. reference was chosen for the reactive power, Q, command. A ramp reference was used to replicate practical application of grid-tied inverters starting up. As seen in the plots, the control loops adequately respond to ramp changes in the active power with minimal overshoot and quick rise time. In steady state, the error is almost entirely removed. This therefore, verifies the functionality of the grid-tied inverter model under normal conditions which will be used for the subsequent nonlinear observer investigation.

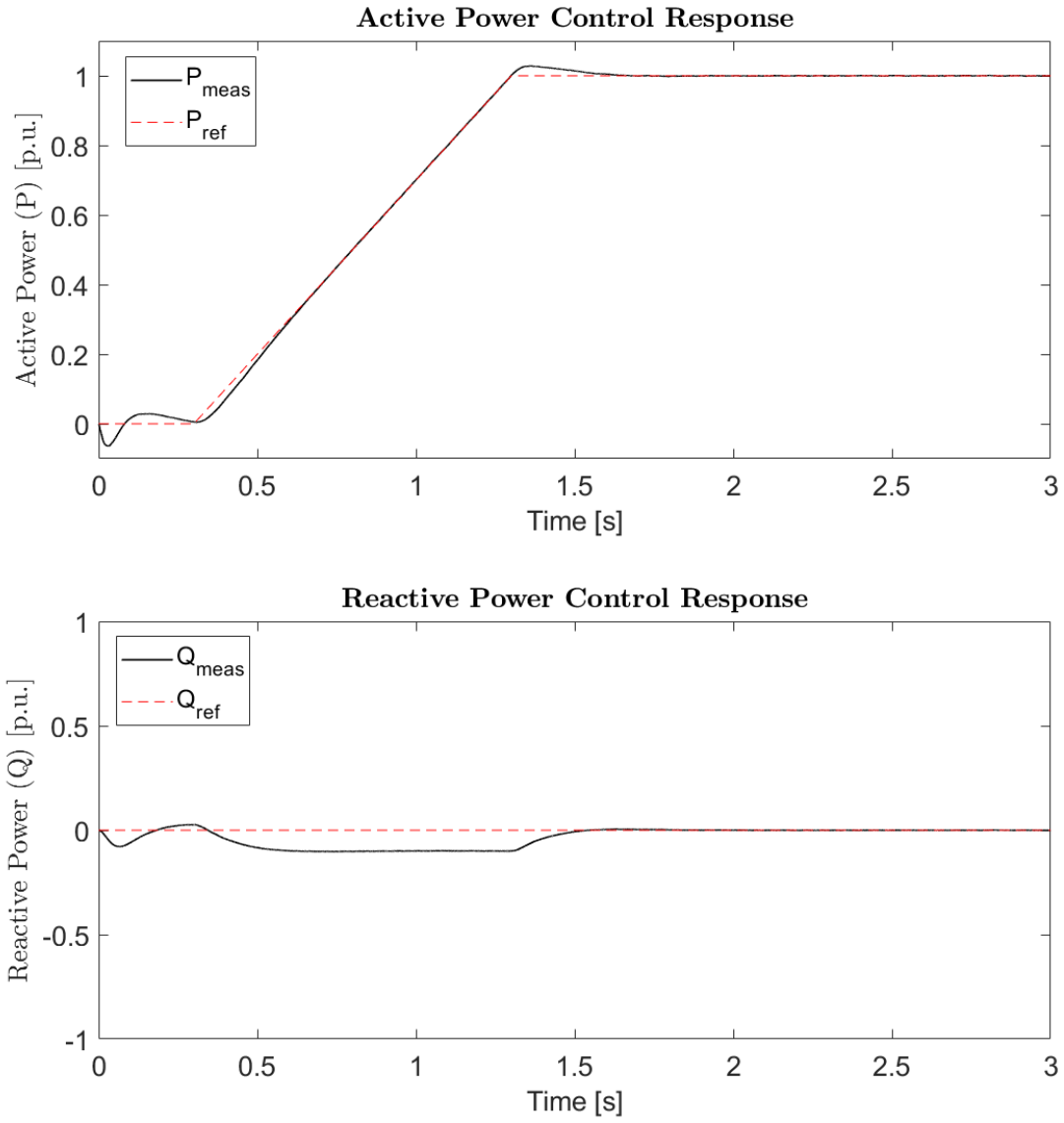

Figure 8: Active and reactive power ramp response, grid-tied inverter control.

2.2.3 Step-Down Transformer

The Δ-Y transformer in the feeder branch provides both an impedance between the sources and loads as well as a phase shift. The inclusion of this transformer is essential to

the model in that it provides enough impedance between the sources and load to minimize source voltage collapse during faults downstream of the transformer. In the Simulation Results chapter, it will be seen that line-to-ground faults upstream of the transformer will collapse the source voltages beyond their operating limits and will cause tripping in the system sources due to loss of voltage faults. The scenario to be explored with the observer is where the voltages do not collapse. Downstream of the transformer and closer in proximity to the load, the source voltages will not collapse entirely due to the transformer impedance along with line impedances which provides an interesting test case scenario. The parameters for the Δ-Y transformer are shown in Table 5.

Table 5: Δ-Y Transformer Parameters

Parameter	**Value**
3 Phase Transformer MVA	45 kVA
Base Operation Frequency	60 Hz
Primary Winding Type	Δ
Secondary Winding Type	Y-GND
Phase Shift	Δ Lags Y
Positive Sequence Leakage Reactance	0.05 p.u.
Primary Winding Line-to-Line Voltage	480 V
Secondary Winding Line-to-Line Voltage	208 V

2.2.4 Line Impedances

To model the system more realistically, cable impedances were added between the sources and main 480 V bus and between fault locations, the transformer, and the fixed load. The inclusion of cable impedances is similar to that of the transformer in that it provides impedance between the sources and load to minimize source voltage collapse during faults in the system. Table 6 provides the positive and zero sequence line impedance parameters per unit length, and Table 7 provides the lengths of each of the five cable sections identified in Fig. 1.

Table 6: Positive and Zero Sequence Line Impedance Parameters

Positive Sequence		**Zero Sequence**	
Parameter	**Value**	**Parameter**	**Value**
$\mathbf{R}_1$	1.32e-4 Ω/m	$\mathbf{R}_0$	4.16e-4 Ω/m
$\mathbf{X}_{L,1}$	8.50e-5 Ω/m	$\mathbf{X}_{L,0}$	2.10e-5 Ω/m
$\mathbf{X}_{C,1}$	10.00e10 $M\Omega$-m	$\mathbf{X}_{C,0}$	10.00e10 $M\Omega$-m

Table 7: Cable Lengths

Cable	**Length** [m]	**Length** [ft]
1	13.72	45
2	13.72	45
3	10.67	35
4	10.67	35
5	10.67	35

2.2.5 Fixed Load

To complete the model, a fixed load was added downstream of the Δ-Y transform. The load is nominally rated at 45 kVA and 0.85 p.f. Altogether, nominally the grid-tied inverter source will produce 30 kW and the grid-forming inverter source will make up the difference producing the remaining active and reactive power required by the load.

3.0 Observer Development

3.1 Motivation

This work proposes the use of a nonlinear observer using a model-based approach for the purpose of fault detection. In control theory, observers can be used to create state information for unmeasurable signals. When the general form of the system model is known, an observer can be utilized to create state information for unmodelled effects, $\hat{F}(t) \in R$, which are present in the system. With respect to our study, in knowing the general form of the grid-tied inverter's dynamic model, $\hat{F}(t)$ can be used to create an unmodelled fault signature in the system. Furthermore, if the general form of the system model is an accurate representation of the system's actual dynamics, under normal operation it is expected that $\hat{F}(t)$ is approximately equal to zero. During abnormal operation or fault conditions, the $\hat{F}(t)$ term is not equal to zero. Therefore, using signals which are already measured and used by the inverter metering and control systems, a fault signature signal can be created. By monitoring changes in this value, a fault could be easily detected by a simple threshold method. The remainder of the section derives the observer.

3.2 Observer Derivation and Equations

Deriving a voltage loop around the filter inductor, the following ideal model equations for the grid-tied inverter in Fig. 7 can be written as

$$L_F \begin{bmatrix} \dot{I}_a \\ \dot{I}_b \\ \dot{I}_c \end{bmatrix} \triangleq \frac{V_{DC}}{2} \begin{bmatrix} m_a \\ m_b \\ m_c \end{bmatrix} - R_F \begin{bmatrix} I_a \\ I_b \\ I_c \end{bmatrix} - V_g \begin{bmatrix} cos(\theta) \\ cos(\theta - \frac{2\pi}{3}) \\ cos(\theta + \frac{2\pi}{3}) \end{bmatrix} \tag{3.1}$$

where L_F and R_F are the filter inductance and resistance, respectively, $V_{DC}(t)$ is the inverter DC input voltage, $V_g(t)$ is the AC side bus voltage, $I_a(t)$, $I_b(t)$, $I_c(t)$, are the phase currents,

and $m_a(t)$, $m_b(t)$, $m_c(t)$, are the inverter control modulation signals. Given the grid-tied inverter system model in (3.1), unmodelled fault signatures, $F_a(t)$, $F_b(t)$, $F_c(t)$, are added to the grid-tied inverter system model as

$$L_F \begin{bmatrix} \dot{I}_a \\ \dot{I}_b \\ \dot{I}_c \end{bmatrix} = \frac{V_{DC}}{2} \begin{bmatrix} m_a \\ m_b \\ m_c \end{bmatrix} - R_F \begin{bmatrix} I_a \\ I_b \\ I_c \end{bmatrix} - V_g \begin{bmatrix} cos(\theta) \\ cos(\theta - \frac{2\pi}{3}) \\ cos(\theta + \frac{2\pi}{3}) \end{bmatrix} + \begin{bmatrix} F_a \\ F_b \\ F_c \end{bmatrix}. \tag{3.2}$$

Before continuing, this observer development necessitates the following assumptions:

- *Assumption 1:* The signals $V_{DC}(t)$, $V_g(t)$, $I_a(t)$, $I_b(t)$, $I_c(t)$, $m_a(t)$, $m_b(t)$, and $m_c(t)$ are measurable.
- *Assumption 2:* The signals $F_a(t)$, $F_b(t)$, and $F_c(t)$ and their first and second derivatives are piecewise continuous and bounded.
- *Assumption 3:* The parameters L_F and R_F are known *a priori* and are assumed to be constant with respect to time.

To simplify the analysis of the three-phase circuit and the control of the observer, the three-phase model is then transformed into the DQ frame. *Motor notation*, defined in [13], is used in which the direct axis is aligned to the A-phase and leads the quadrature axis by 90°, giving

$$L_F \begin{bmatrix} \dot{I}_d \\ \dot{I}_q \end{bmatrix} = \frac{V_{DC}}{2} \begin{bmatrix} m_d \\ m_q \end{bmatrix} - \begin{bmatrix} R_F & \omega L_F \\ -\omega L_F & R_F \end{bmatrix} \begin{bmatrix} I_d \\ I_q \end{bmatrix} - \begin{bmatrix} V_{gd} \\ V_{gq} \end{bmatrix} + \begin{bmatrix} F_d \\ F_q \end{bmatrix}. \tag{3.3}$$

The goal is to design nonlinear observers for $F_d(t)$ and $F_q(t)$, denoted $\hat{F}_d(t)$ and $\hat{F}_q(t)$, such that $\hat{F}_d(t) \rightarrow F_d(t)$ and $\hat{F}_q(t) \rightarrow F_q(t)$ as t $\rightarrow \infty$ with rapid convergence. With the proper design of the observer, the subsequently defined error signals of the observer will converge to zero. During a fault condition, $F_d(t)$ and $F_q(t)$ will become non-zero as this is an indication of unmodelled characteristics in the dynamic model. The observer signals $\hat{F}_d(t)$ and $\hat{F}_q(t)$ will learn the fault signature, hence driving these error signals to zero as proved by the subsequent stability analysis in [14]. These observers signals can be utilized as an indication

of the fault event. With this motivation, by solving (3.3), the observers, $\dot{\hat{I}}_d(t)$ and $\dot{\hat{I}}_q(t)$, can be designed as

$$\begin{bmatrix} \dot{\hat{I}}_d \\ \dot{\hat{I}}_q \end{bmatrix} \triangleq \frac{1}{L_F}\left(\frac{V_{DC}}{2} \begin{bmatrix} m_d \\ m_q \end{bmatrix} - \begin{bmatrix} R_F & \omega L_F \\ -\omega L_F & R_F \end{bmatrix} \begin{bmatrix} I_d \\ I_q \end{bmatrix} - \begin{bmatrix} V_{gd} \\ V_{gq} \end{bmatrix} + \begin{bmatrix} \hat{F}_d \\ \hat{F}_q \end{bmatrix} \right) \tag{3.4}$$

where $\hat{F}_d(t)$ and $\hat{F}_q(t)$ are the observed fault signals. These current observer signals are then used to create the D-axis and Q-axis observer error signals defined as

$$\begin{bmatrix} e_d \\ e_q \end{bmatrix} \triangleq \begin{bmatrix} I_d \\ I_q \end{bmatrix} - \begin{bmatrix} \hat{I}_d \\ \hat{I}_q \end{bmatrix}. \tag{3.5}$$

Similar to the fault terms, the goal of the observer is such that $e_d(t)$ and $e_q(t) \to 0$ as $t \to \infty$. Taking the derivative of (3.5) and substituting in (3.3) and (3.4), it is found that

$$\begin{bmatrix} \dot{e}_d \\ \dot{e}_q \end{bmatrix} = \frac{1}{L_F}\left(\begin{bmatrix} F_d \\ F_q \end{bmatrix} - \begin{bmatrix} \hat{F}_d \\ \hat{F}_q \end{bmatrix} \right) = \frac{1}{L_F} \begin{bmatrix} \tilde{F}_d \\ \tilde{F}_q \end{bmatrix}. \tag{3.6}$$

Auxiliary error signals are then defined to facilitate closed-loop observer development as

$$\begin{bmatrix} s_d \\ s_q \end{bmatrix} \triangleq \begin{bmatrix} \dot{e}_d \\ \dot{e}_q \end{bmatrix} + \begin{bmatrix} e_d \\ e_q \end{bmatrix} \tag{3.7}$$

$$\begin{bmatrix} \dot{s}_d \\ \dot{s}_q \end{bmatrix} = \begin{bmatrix} \ddot{e}_d \\ \ddot{e}_q \end{bmatrix} + \begin{bmatrix} \dot{e}_d \\ \dot{e}_q \end{bmatrix}. \tag{3.8}$$

As before, the goal of the observer is such that $s_d(t)$ and $s_q(t) \to 0$ as $t \to \infty$. Using the derivative of (3.6) and substituting into (3.8), the following can be obtained as

$$\begin{bmatrix} \dot{s}_d \\ \dot{s}_q \end{bmatrix} = \frac{1}{L_F}\left(\begin{bmatrix} \dot{F}_d \\ \dot{F}_q \end{bmatrix} - \begin{bmatrix} \dot{\hat{F}}_d \\ \dot{\hat{F}}_q \end{bmatrix} \right) + \begin{bmatrix} \dot{e}_d \\ \dot{e}_q \end{bmatrix}. \tag{3.9}$$

Motivated by a Lyapunov stability analysis in [14], the fault observer terms can then be defined as

$$\begin{bmatrix} \dot{\hat{F}}_d \\ \dot{\hat{F}}_q \end{bmatrix} \triangleq (k_1 + 1) \begin{bmatrix} s_d \\ s_q \end{bmatrix} + k_2 sgn\left(\begin{bmatrix} e_d \\ e_q \end{bmatrix} \right) \tag{3.10}$$

where k_1, $k_2 \in R$ are positive control gains and sgn$(\cdot)$ is the signum function. Finally, by integrating, an implementable form of the observer which can be used in the PSCAD model results and is

$$\hat{F} = (k_1 + 1)\left(e(t) - e(t_0) + \int_{t_0}^{t} e(\sigma) d\sigma \right) + k_2 \int_{t_0}^{t} sgn(e(\sigma)) d\sigma. \tag{3.11}$$

3.3 Stability Analysis

The result of (3.10) is motivated by a Lyapunov stability analysis done in [14]. For completeness, the stability analysis from [14] is modified for the DQ-frame analysis with the filter inductance and replicated here in this document. Note that the following analysis is shown without the d or q subscripts, and is true for both subsystems.

Theorem 1: The fault observer in (3.10) ensures that $e(t)$ and $s(t) \to 0$ as $t \to \infty$.

Proof: A non-negative Lyapunov function $V(t) \in R$ is defined as

$$V = \frac{1}{2}e^2 + \frac{1}{2}s^2, \tag{3.12}$$

for which the derivative is

$$\dot{V} = e\dot{e} + s\dot{s}. \tag{3.13}$$

Solving (3.7) for $\dot{e}$ and substituting it alongside (3.9) into (3.13) and simplifying results in

$$\dot{V} = s^2 - e^2 + \frac{s}{L_F}(\dot{F} - \dot{\hat{F}}). \tag{3.14}$$

Substituting in (3.10) and rearranging results in

$$\dot{V} = -e^2 - \frac{k_1}{L_F}s^2 + \frac{\dot{e}}{L_F}\dot{F} - \frac{\dot{e}}{L_F}k_2 sgn(e) + \frac{e}{L_F}\Big(\dot{F} - k_2 sgn(e)\Big). \tag{3.15}$$

Integrating both sides of (3.15) yields

$$V \leq V(t_0) + I_1 - I_2 + I_3 - I_4 \tag{3.16}$$

where

$$I_1 = \frac{1}{L_F}\int_{t_0}^{t} \dot{e}(\sigma)\dot{F}(\sigma)d\sigma, \tag{3.17}$$

$$I_2 = \frac{k_2}{L_F}sgn(e)\int_{t_0}^{t} e(\sigma)d\sigma, \tag{3.18}$$

$$I_3 = \frac{1}{L_F}\int_{t_0}^{t} e(\sigma)\Big(\dot{F}(\sigma) - k_2 sgn(e(\sigma))\Big)d\sigma, \tag{3.19}$$

$$I_4 = \int_{t_0}^{t} e^2(\sigma)d\sigma + \frac{k_1}{L_F}\int_{t_0}^{t} s^2(\sigma)d\sigma, \tag{3.20}$$

and $V(t_0)$ is the initial value of $V(t)$. Using integration by parts on (3.17) results in

$$I_1 = \frac{1}{L_F}\left[e(t)\dot{(}F)(t) - e(t_0)\dot{F}(t_0) - \int_{t_0}^{t} e(\sigma)\ddot{F}(\sigma)d\sigma\right] \tag{3.21}$$

and evaluating (3.18) yields

$$I_2 = \frac{k_2}{L_F}sgn(e(t))e(t) - \frac{k_2}{L_F}sgn(e(t_0))e(t_0). \tag{3.22}$$

Substituting (3.21) and (3.22) into (3.16) and simplifying results in

$$V \leq -\int_{t_0}^{t} e^2(\sigma)d\sigma - \frac{k_1}{L_F}\int_{t_0}^{t} s^2(\sigma)d\sigma + C_0 \tag{3.23}$$

where

$$C_0 = V(t_0) - \frac{e(t_0)}{L_F}\left(\dot{F}(t_0) - k_2 sgn(e(t_0))\right). \tag{3.24}$$

From the structure of (3.23) and the definition of (3.24), it can then be said that $V(t) \in \mathcal{L}_\infty$; hence, $e(t), s(t) \in \mathcal{L}_\infty$. From this, it can then be said from the form of (3.7) that $\dot{e} \in \mathcal{L}_\infty$. From the form of (3.10) it is then true that $\dot{\hat{F}} \in \mathcal{L}_\infty$. Looking at (3.9), using *Assumption 2* it can be said that $\dot{s} \in \mathcal{L}_\infty$. Since $e, \dot{e}, s, \dot{s} \in \mathcal{L}_\infty$, then Barbalat's Lemma can be used to prove that $|e(t)|$ and $|s(t)| \to 0$ as $t \to \infty$.

3.4 Implementation

To emphasize the location of the nonlinear observers in the system, Fig. 9 shows the system level nonlinear fault observer implementation. Important to note, the nonlinear observer acts as an embedded system to the grid-tied inverter. Utilizing only the signals already measured and used by standard grid-tied inverters, the implementation of the nonlinear observers is simple. Namely, L_F and R_F are the filter inductance and resistance respectively and are known values. $V_{DC}(t)$ is the inverter DC input voltage and is already measured by the grid-tied inverter. $V_g(t)$ is the AC side bus voltage, and $I_a(t)$, $I_b(t)$, and $I_c(t)$ are the phase currents which all are monitored and measured. Finally $m_a(t)$, $m_b(t)$, and $m_c(t)$ are the inverter control modulation signals. These signals are already created to produce the output AC waveform and can be inputted into the observer system. Evidently, the nonlinear

observer requires no new signals, which is a major advantage to this approach. Hence, as seen in the figure, the observer would be embedded within the grid-tied inverter. The observer then only sees what the grid-tied inverter measures within its own control system and at its terminals. This simplifies the solution as well because the nonlinear observers do not require anything external to the inverter, making this a completely internal solution while the remainder of the system can be a "black box" and no other information is required to be known.

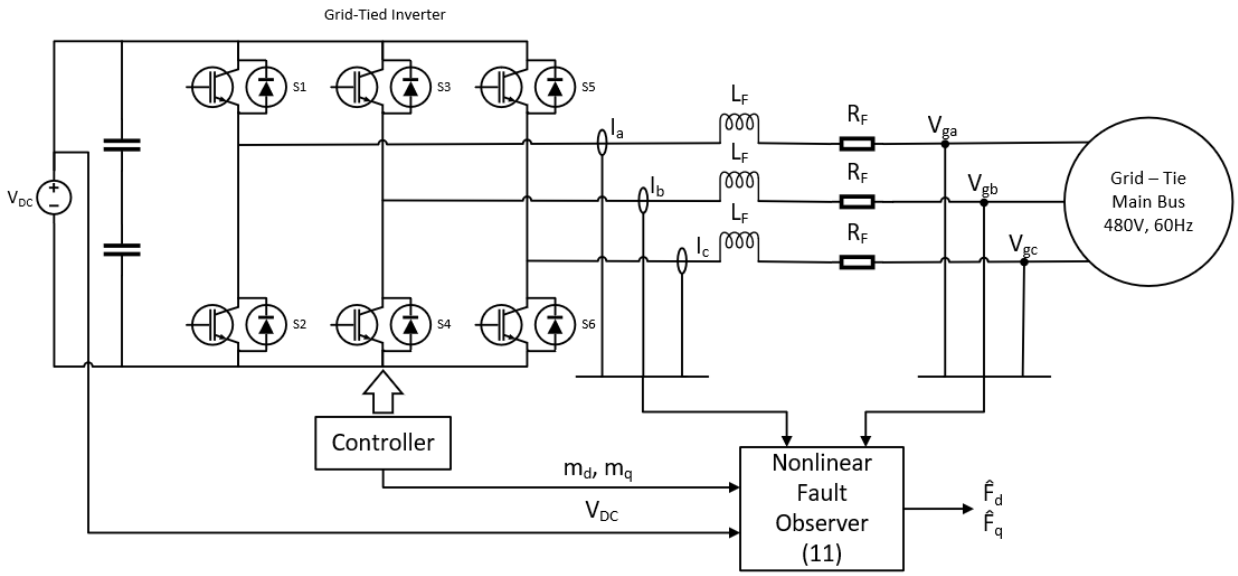

Figure 9: Nonlinear observer embedded within grid-tied inverter.

Diving deeper into the Nonlinear Fault Observer block in Fig. 9, the equation in (3.11) shows the general implementable form of the nonlinear observers which can be easily implemented in the PSCAD simulation environment with standard blocks. Figs. 10 and 11 show the control block diagrams for both the D-axis and Q-axis nonlinear observers. It is important to note that integrator time constants were set to one second and a second order Butterworth filter was used to preprocess the modulation signals due to their high harmonic content. This filtering aided with the observer control system and would likely be used in a real implementation of the system to filter out noise. The other remaining six signals would also likely have some filtering as well, although not required in the simulation environment.

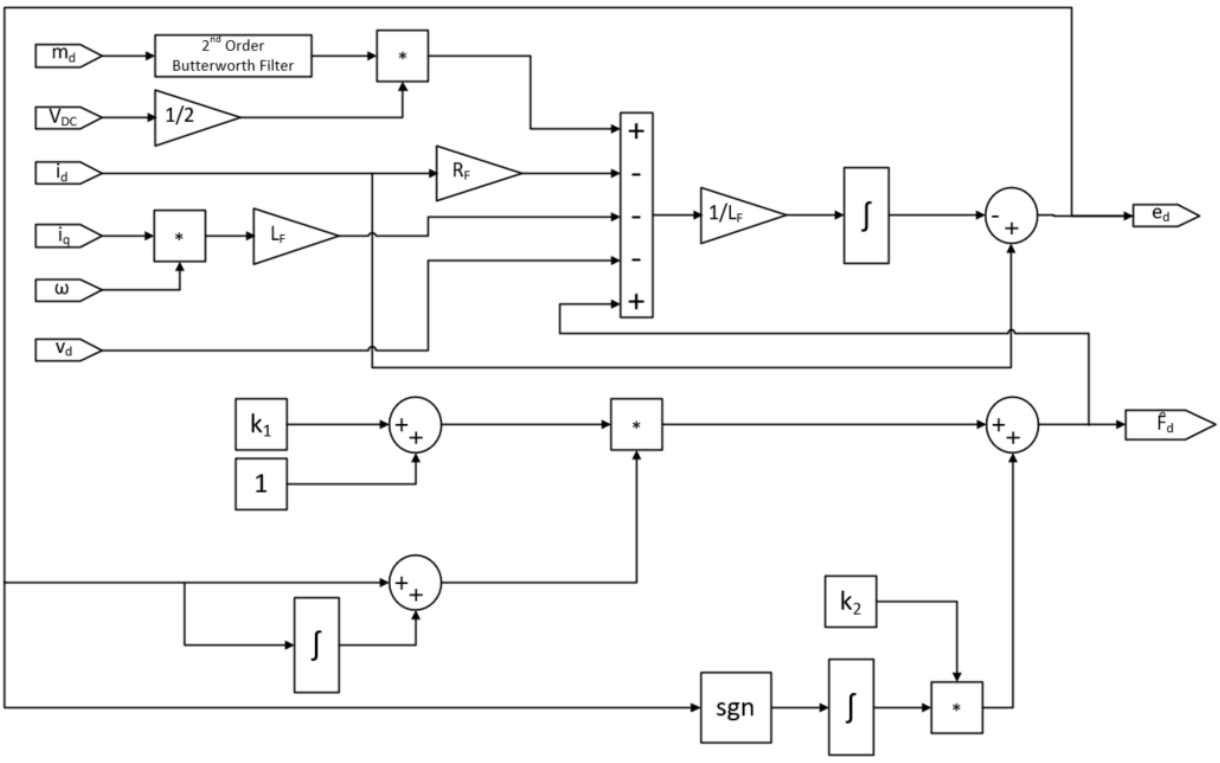

Figure 10: D-Axis nonlinear observer embedded within grid-tied inverter.

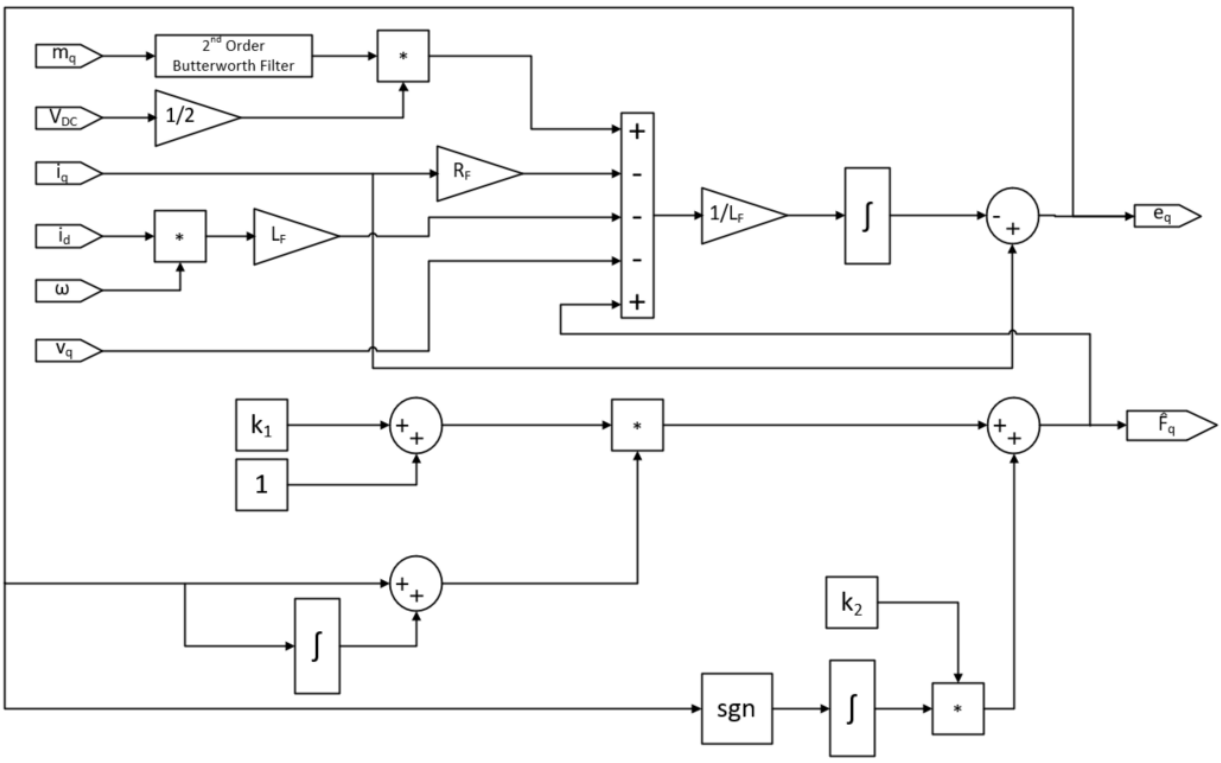

Figure 11: Q-Axis nonlinear observer embedded within grid-tied inverter.

Table 8 provides the important parameters for both the D-axis and Q-axis nonlinear observers. The gains for the observer were chosen experimentally to provide fast settling times and to minimize steady state error. Filter resistance and inductance were chosen from typical inverter filter values.

Table 8: D-Axis and Q-Axis Nonlinear Observer Parameters

Parameter	**Value**
k_1	5
k_2	600
R_F	0.1 Ω
L_F	0.010 H

4.0 Simulation Results

To investigate and validate the effectiveness of the observer developed in the previous section, simulations were generated using PSCAD simulation software. A sensitivity analysis was carried out with twelve test cases in which both single line-to-ground and line-to-line faults were simulated at each of the four fault bus locations shown in Fig. 1. Figs. 12, 13, and 14 present plots of one of the test cases: a single line-to-ground fault in phase A at fault location A (the load bus).

In Fig. 12, plots of the grid-tied inverter current and voltage are presented. The fault occurs at 2.5 seconds, and the system is in steady state beforehand. It is important to note that under fault, the grid-tied inverter current remains in the range of 1.0 to 1.5 p.u. and the voltage levels do not entirely collapse, remaining around +/- 15% the nominal voltage in p.u. This is the expected fault behavior of the modelled system, in which the system sources operate at close to nominal levels of current and voltage under faulted conditions. Traditional circuit protection methods will likely fail to operate in these conditions.

The strength of this observer technique is seen in Fig. 14, which depicts the $\hat{F}_d(t)$ and $\hat{F}_q(t)$ fault observer signals. The $\hat{F}_d(t)$ and $\hat{F}_q(t)$ terms are approximately zero under steady state conditions as the ideal inverter equations model the system adequately. Important to note, the error terms, $e_d(t)$ and $e_q(t)$ of (3.5), are also close to zero (less than 2 A) under normal circumstances as seen in Fig. 13, supporting the mathematical development and proof of the observer. When the fault occurs at 2.5 seconds, the fault observer terms grow rapidly to large magnitudes relative to the steady state value within the first few cycles and remain throughout the duration of the fault. In this fault scenario, the change in magnitudes of $\hat{F}_d(t)$ and $\hat{F}_q(t)$ from steady state to fault was 103 V and 137 V, respectively. Both the magnitude and speed of the response show the effectiveness of this technique to providing insight into unmodelled signatures present in the system.

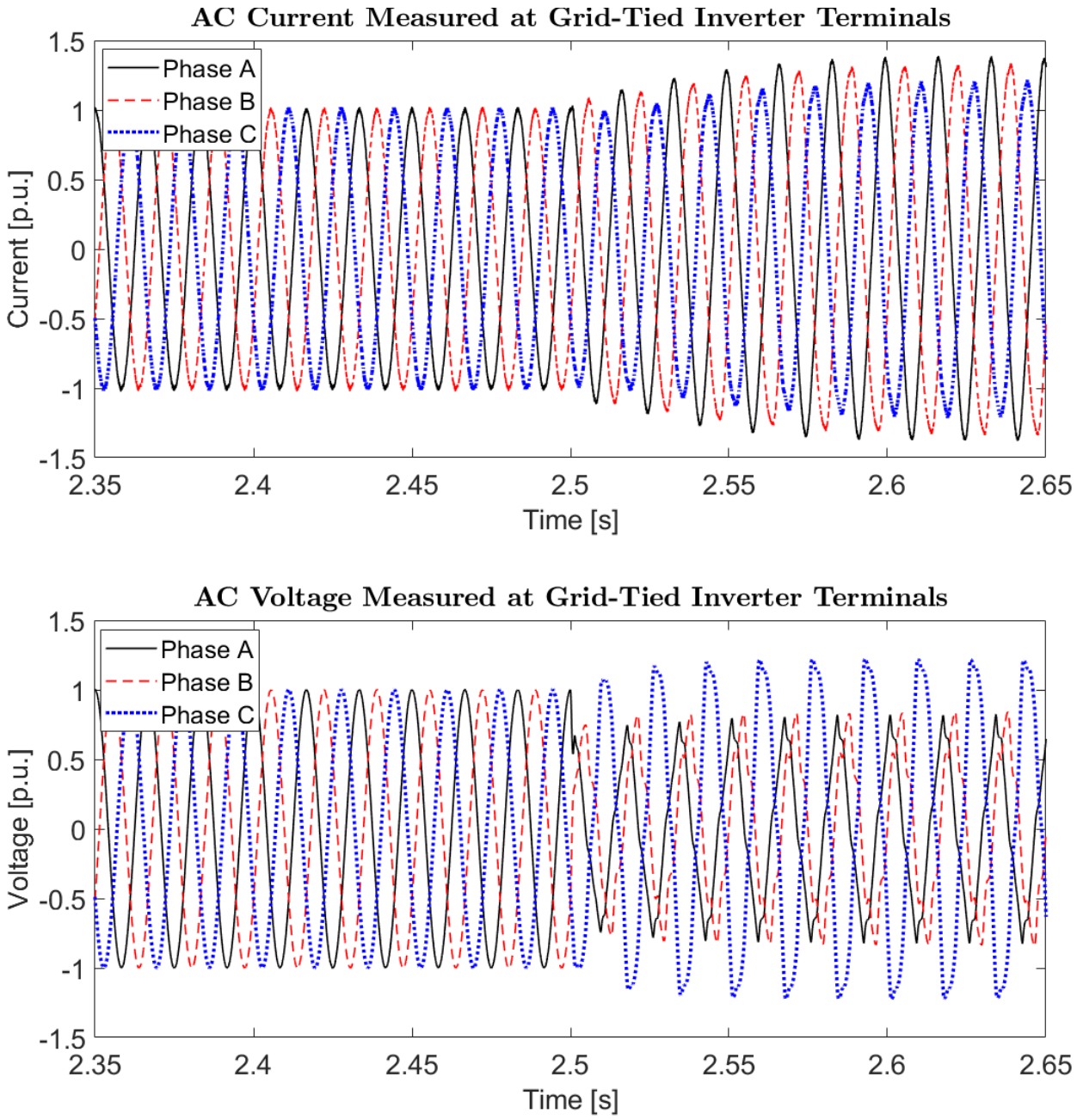

Figure 12: AC current (top) and voltage (bottom) measured at grid-tied inverter terminals during Phase A to Ground fault at bus location A occurring at 2.5 seconds.

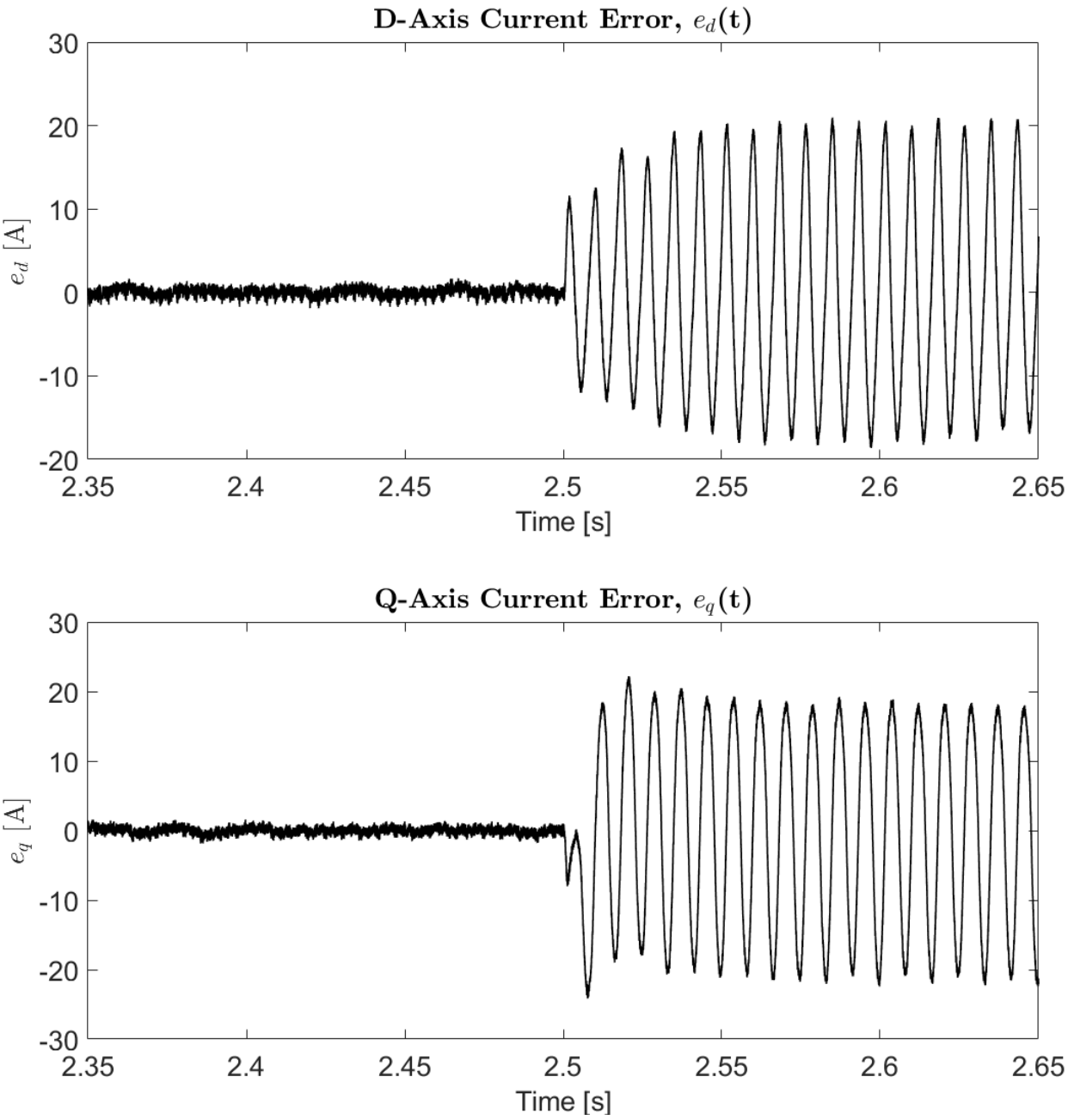

Figure 13: D-axis current error, $e_d(t)$, (top) and Q-axis current error, $e_d(t)$, (bottom) during Phase A to Ground fault at bus location A occurring at 2.5 seconds.

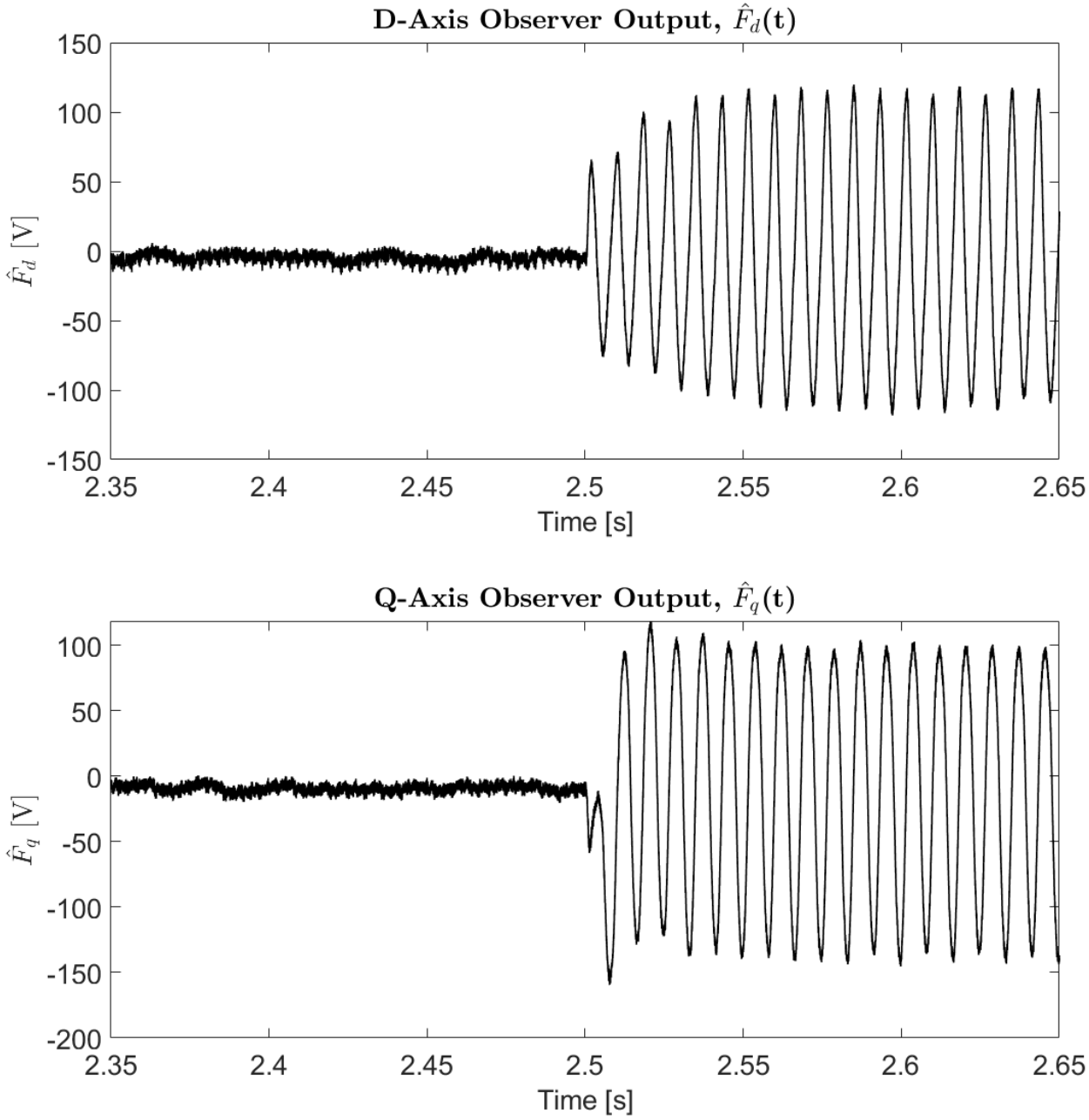

Figure 14: D-axis observer output, $\hat{F}_d(t)$, (top) and Q-axis observer output, $\hat{F}_q(t)$, (bottom) during Phase A to Ground fault at bus location A occurring at 2.5 seconds.

The parameters $\Delta\hat{F}_d$ and $\Delta\hat{F}_q$ are then defined as the magnitude of the difference between the values of $\hat{F}_d(t)$ and $\hat{F}_q(t)$ during steady state conditions and under faulted conditions, resulting in

$$\Delta\hat{F}_d = |\hat{F}_{d,fault} - \hat{F}_{d,ss}| \tag{4.1}$$

$$\Delta\hat{F}_q = |\hat{F}_{q,fault} - \hat{F}_{q,ss}|. \tag{4.2}$$

Table 9 summarizes the results of the twelve trials with the value of the output parameters, $\Delta\hat{F}_d$ and $\Delta\hat{F}_q$. Other data from the twelve trials can be found in the Appendix: Fault Trial Data. As seen in the table, the observer performs well for both single line-to-ground faults and line-to-line faults at the multiple fault locations tested. The resultant observed terms create a large enough change that a simple threshold algorithm could be used to identify when a fault has occurred.

Table 9: Fault Sensitivity Analysis

Fault Type	**Fault Location**	$\Delta\hat{F}_d$ **(V)**	$\Delta\hat{F}_q$ **(V)**
A-GND	A	103	137
B-GND	A	108	146
C-GND	A	103	141
A-GND	B	132	169
A-GND	C	14	50
A-GND	D	15	53
A-B	A	149	187
B-C	A	153	193
C-A	A	154	162
A-B	B	176	213
A-B	C	188	215
A-B	D	198	219

The two outliers in the data are the single line-to-ground fault cases at locations C and D. As mentioned in the model development section, the closer the fault is to the main 480 V bus, the greater the impact on the phase voltage under fault, as a fault at the main bus would ground the phase under fault resulting in a voltage of approximately zero volts. At locations C and D, the phase A voltages are less than 0.05 p.u. nominal voltage during the fault. In this case, both inverters would have likely tripped due to loss of voltage on a phase, as this type of event is something in which typical inverters are already programmed to fault. Therefore, the effectiveness of the observer in these cases is not relevant.

5.0 Conclusions

In this thesis, a nonlinear observer is proposed to detect AC faults in heavily-inverter based power systems and microgrids. In these systems, the magnitudes of fault currents are relatively close to nominal currents which would otherwise remain undetected by traditional circuit protection schemes and techniques. A model-based approach that utilizes the assumed dynamics of the grid-tied inverter along with a nonlinear observer provides a novel solution to detect system abnormalities and faults.

Through simulation in the PSCAD simulation environment, it has been verified that the observer technique achieved the three main goals:

- This observer provides insight into unmodelled signatures present in the system.
- These signatures can be utilized to identify faults in the system creating a detection scheme.
- This method requires no additional sensor other than those already required by the grid-tied inverter.

The last point above shows the primary advantage of this observe technique. The observer calculation only requires measurements that are already commonly used in grid-tied inverter metering and control systems and could easily be implemented in an existing system. Furthermore, the calculated output parameter $\Delta\hat{F}$ provides a simple means of detecting faults. Through a simple magnitude threshold algorithm, faults can be identified as producing a $\Delta\hat{F}$ value above a certain threshold. The strength of the technique is in its simplicity and ease of use.

Appendix Fault Trial Data

This section contains relevant data from the twelve fault simulations. In Table 10, the per unit values of the grid-tied inverter peak voltages and currents in each of the three phases under fault are shown for each of the twelve cases.

Table 10: Grid-Tied Inverter Peak Voltages and Currents Under Fault

		Peak Voltage [p.u]			**Peak Current [p.u]**		
Fault Type	**Fault Location**	$\mathbf{V}_a$	$\mathbf{V}_b$	$\mathbf{V}_c$	$\mathbf{I}_a$	$\mathbf{I}_b$	$\mathbf{I}_c$
A-GND	A	0.825	0.847	1.220	1.389	1.339	1.217
B-GND	A	1.229	0.829	0.846	1.213	1.384	1.342
C-GND	A	0.847	1.221	0.825	1.339	1.216	1.381
A-GND	B	0.769	0.814	1.344	1.553	1.479	1.267
A-GND	C	0.026	1.652	1.795	1.026	1.033	1.018
A-GND	D	0.017	1.660	1.805	1.025	1.032	1.020
A-B	A	1.221	0.362	1.150	1.497	1.630	1.436
B-C	A	1.160	1.223	0.360	1.428	1.501	1.628
C-A	A	0.361	1.152	1.222	1.623	1.426	1.487
A-B	B	1.254	0.281	1.275	1.654	1.799	1.554
A-B	C	0.760	0.690	1.452	2.091	2.041	1.515
A-B	D	0.751	0.701	1.452	2.252	2.170	1.558

In Table 11, the per unit values of the grid-forming inverter peak voltages and currents in each of the three phases under fault are shown for each of the twelve cases.

Table 11: Grid-Forming Inverter Peak Voltages and Currents Under Fault

		Peak Voltage [p.u]			**Peak Current [p.u]**		
Fault Type	**Fault Location**	$\mathbf{V}_a$	$\mathbf{V}_b$	$\mathbf{V}_c$	$\mathbf{I}_a$	$\mathbf{I}_b$	$\mathbf{I}_c$
A-GND	A	0.825	0.847	1.220	1.282	1.411	0.900
B-GND	A	1.228	0.829	0.846	0.889	1.283	1.413
C-GND	A	0.847	1.220	0.825	1.409	0.893	1.287
A-GND	B	0.769	0.814	1.344	1.281	1.410	1.084
A-GND	C	0.026	1.652	1.795	0.219	0.470	0.281
A-GND	D	0.017	1.659	1.805	0.228	0.470	0.282
A-B	A	1.222	0.361	1.150	0.850	1.425	1.379
B-C	A	1.159	1.222	0.360	1.390	0.841	1.420
C-A	A	0.361	1.152	1.221	1.421	1.388	0.841
A-B	B	1.254	0.281	1.275	1.015	1.419	1.409
A-B	C	0.760	0.690	1.451	1.248	1.415	1.266
A-B	D	0.750	0.701	1.452	1.243	1.427	1.294

Table 12 provides the complete data set of current error values, e_d and e_q, and unmodelled fault characteristic terms, $\hat{F}_d$ and $\hat{F}_q$ for each of the twelve trials during the steady state period.

Table 12: Steady State Observer Error and $\hat{F}$ Complete Trial Data

		D-Axis		**Q-Axis**	
Fault Type	**Fault Location**	e_d **[A]**	$\hat{F}_d$ **[V]**	e_q **[A]**	$\hat{F}_q$ **[V]**
A-GND	A	2.0	17.1	1.9	22.2
B-GND	A	2.0	17.1	1.9	22.2
C-GND	A	2.0	17.1	1.9	22.2
A-GND	B	2.1	19.0	2.0	20.7
A-GND	C	2.0	17.6	2.1	22.1
A-GND	D	1.9	16.5	2.0	21.0
A-B	A	2.0	17.1	1.9	22.2
B-C	A	2.0	17.1	1.9	22.2
C-A	A	2.0	17.1	1.9	22.2
A-B	B	2.0	19.0	1.9	19.8
A-B	C	2.0	17.6	2.1	22.1
A-B	D	1.9	16.5	1.9	20.7

Table 13 provides the complete data set of current error values, e_d and e_q, and unmodelled fault characteristic terms, $\hat{F}_d$ and $\hat{F}_q$ for each of the twelve trials during the fault period.

Table 13: Observer Error and $\hat{F}$ Under Fault Complete Trial Data

		D-Axis		**Q-Axis**	
Fault Type	**Fault Location**	e_d **[A]**	$\hat{F}_d$ **[V]**	e_q **[A]**	$\hat{F}_q$ **[V]**
A-GND	A	21.0	119.9	24.1	159.5
B-GND	A	21.7	124.7	25.8	167.8
C-GND	A	21.0	120.5	25.3	163.2
A-GND	B	24.4	151.3	29.3	189.9
A-GND	C	4.6	31.8	10.6	72.5
A-GND	D	4.5	31.3	10.6	73.5
A-B	A	26.6	166.2	32.5	209.1
B-C	A	27.2	170.5	33.7	214.7
C-A	A	27.3	171.2	29.0	184.6
A-B	B	31.1	194.7	37.0	233.3
A-B	C	33.4	206.0	37.3	237.6
A-B	D	34.7	214.0	37.5	239.5

Bibliography

[1] H. A. Al Hassan, Q. Fu, V. Bharavaju, Y. Yang and B. M. Grainger, "High-speed algorithm for renewable energy based microgrid fault detection and protective coordination," *2017 IEEE Energy Conversion Congress and Exposition (ECCE)*, Cincinnati, OH, 2017, pp. 519-525.

[2] G. Kou, L. Chen, P. VanSant, F. Velez-Cedeno and Y. Liu, "Fault Characteristics of Distributed Solar Generation," in *IEEE Transactions on Power Delivery*, vol. 35, no. 2, pp. 1062-1064, April 2020.

[3] Q. Zhong and G. Weiss, "Synchronverters: Inverters That Mimic Synchronous Generators," in *IEEE Transactions on Industrial Electronics*, vol. 58, no. 4, pp. 1259-1267, April 2011.

[4] H. Nikkhajoei and R. H. Lasseter, "Microgrid Protection," *2007 IEEE Power Engineering Society General Meeting*, Tampa, FL, USA, 2007, pp. 1-6.

[5] R. Escudero, J. Noel, J. Elizondo and J. Kirtley, "Microgrid fault detection based on wavelet transformation and Park's vector approach," *Electric Power Systems Research*, vol. 152, 2017, Pages 401-410.

[6] M. Brucoli, T. C. Green and J. D. F. McDonald, "Modelling and Analysis of Fault Behaviour of Inverter Microgrids to Aid Future Fault Detection," *2007 IEEE International Conference on System of Systems Engineering*, San Antonio, TX, USA, 2007, pp. 1-6.

[7] S. Hossain-McKenzie, E. Piesciorovsky, M. Reno and J. Hambrick, "Microgrid Fault Location: Challenges and Solutions," June 2018.

[8] S. A. Morello, H. A. Al Hassan, B. G. Campbell, R. J. Kerestes and G. F. Reed, "Upstream Fault Detection Using Second Harmonic Magnitudes in a Grid Tied Microgrid Setting," *2018 IEEE Power & Energy Society General Meeting (PESGM)*, Portland, OR, 2018, pp. 1-5.

[9] E. Sortomme, M. Venkata and J. Mitra, "Microgrid protection using communication-assisted digital relays," *IEEE PES General Meeting*, Minneapolis, MN, USA, 2010, pp. 1-1.

[10] W. H. Kersting, *Distribution System Modeling and Analysis*, 4th ed. Boca Raton, FL: CRC Press, 2017.

[11] J. Rocabert, A. Luna, F. Blaabjerg and P. Rodríguez, "Control of Power Converters in AC Microgrids," in *IEEE Transactions on Power Electronics*, vol. 27, no. 11, pp. 4734-4749, Nov. 2012.

[12] A. Yazdani and R. Iravani, *Voltage-Sourced Converters in Power Systems: Modeling, Control, and Applications*, 1st ed. Hoboken: Wiley, 2010.

[13] C. -M. Ong, *Dynamic Simulations of Electric Machinery: Using MATLAB/SIMULINK*. Prentice Hall, 1997.

[14] N. Hawkins, N. Jewell, M. Alqatamin, B. Bhagwat and M. McIntyre, "A Nonlinear Fault Detection Scheme for PV Applications," *2020 American Control Conference (ACC)*, Denver, CO, USA, 2020, pp. 3188-3192.